Optical waveguiding in individual nanometer-scale organic fibers

F. Balzer
Humboldt-Universität zu Berlin, Institut für Physik, D-10115 Berlin, Germany

V. G. Bordo
Prokhorov General Physics Institute, Russian Academy of Sciences, 119991 Moscow, Russia

A. C. Simonsen and H.-G. Rubahn*
Fysisk Institut, Syddansk Universitet, DK-5230 Odense M, Denmark

(Received 27 June 2002; revised manuscript received 3 October 2002; published 17 March 2003)

We show by a combination of spectrally resolved fluorescence and atomic force microscopy that individual, single crystalline, needlelike aggregates of hexaphenyl molecules with submicron cross-sectional dimensions act as optical waveguides (''nanofibers'') in the blue spectral range. The nanofibers are formed via laser-supported, dipole-assisted self-assembly on single crystalline mica substrates. This method allows us to modify the morphology of individual aggregates as well as their mutual distances and the overall orientation of needle arrays. An analytical theory describes quantitatively the waveguiding behavior. From measurements of the damping of propagating 425-nm light the imaginary part of the dielectric function of individual nanoscaled organic aggregates is determined.

DOI: 10.1103/PhysRevB.67.115408 PACS number(s): 78.55.−m, 78.67.−n, 81.07.−b

I. INTRODUCTION

Organic molecules with delocalized π electrons makeup promising new materials for future submicron-sized optoelectronics. They often show large, polarized luminescence efficiencies and have the ability to self-assemble into highly ordered structures on particular substrates or prestructured substrate templates. Hence, one could envision a combination of lithographical techniques and self-assembly to generate customized components which buildup an ordered array of connecting nanoscaled fibers.

Waveguiding all-optical connectors or filters are thus crucial building blocks for future organic optoelectronics. The lithographical approach to obtain elements of that kind is the generation of photonic band-gap structures.[1,2] Here, we present an alternative approach, namely, submicron-sized, single crystalline, and waveguiding nanofibers, grown via laser-assisted self-assembly of *para*-hexaphenyl (*p*-6P) molecules on dielectric substrates.[3] *Para*-hexaphenyl is an oligomer of the conjugated polymer, poly-paraphenylene. It consists of a linear chain of six phenyl rings and has a band gap of 3.2 eV, cf. Fig. 1. The vibronic $S_1 \rightarrow S_0$ exciton spectrum in the solid state is dominated by intense Raman active modes, which are due to C-C stretching vibrations of all carbon atoms of the molecule.

Thin films of *para*-oligophenylenes have been thoroughly investigated in the past[4] since those molecules are candidates for the optically active elements in organic light-emitting diodes, full color displays or organic semiconductor lasers.[5] Adsorbed on dielectric surfaces, the molecular axis is aligned either parallel or normal to the surface, which influences light absorption, emission, and electrical properties.[6] The alignment can be altered by varying adsorption rate and surface temperature in combination with the choice of the underlying substrate (for example, different alkali halides or mica).

We have found that the oligophenylenes grown on a mica substrate form mutually well-oriented aggregates with large aspect ratios: they possess submicron-sized widths and heights but lengths up to millimeters.[7] More elaborate low-energy electron diffraction (LEED) investigations show that their $(1\bar{1}\bar{1})$ faces are oriented parallel to the surface plane.[8] Note that in addition to the $(1\bar{1}\bar{1})$ face the $(2\bar{1}\bar{1})$ face has been observed on mica by a x-ray-diffraction technique.[9] Because of the very similar surface lattice parameters, we cannot distinguish between these two lattices using the LEED apparatus. The aggregates consist of parallel stacks of laying molecules, which are oriented along the direction of microscopic dipoles on the mica surface. The driving force behind the oriented growth is a dipole-induced dipole interaction.

The growth of nanofibers on mica substrates occurs in a rather narrow surface temperature range $\Delta T \approx 25$ K at a small deposition rate of 0.025 nm/s. This allows us to locally induce or avoid needle growth via laser-induced surface heating.[10] The laser manipulation does not change the direction of the needles which is given by the direction of surface dipoles and it does not lower the degree of mutual alignment. However, the length distribution as well as the distances between nanofibers can be varied by changing the ratio between global and local heating.

In the present paper, we take advantage of these growth parameters to manipulate the needle formation in order to investigate the waveguiding properties of *individual* nanofibers. We select nanofibers with interesting morphological

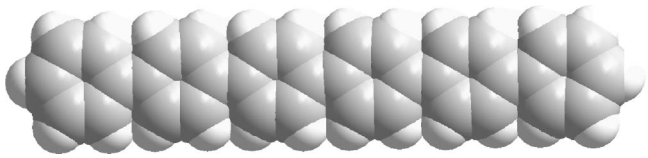

FIG. 1. Space-filling model of a *p*-6P molecule.

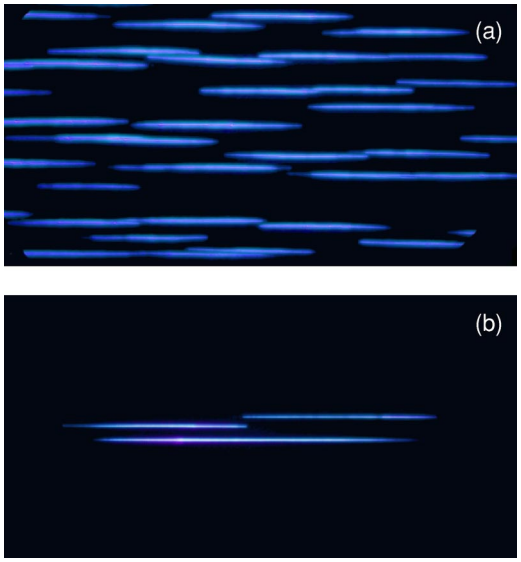

FIG. 2. Fluorescence images of well isolated hexaphenyl needles on mica. (a) 180×350 μm^2; needle length 100 ± 20 μm. (b) 230×450 μm^2; needle lengths 170 and 280 μm, respectively.

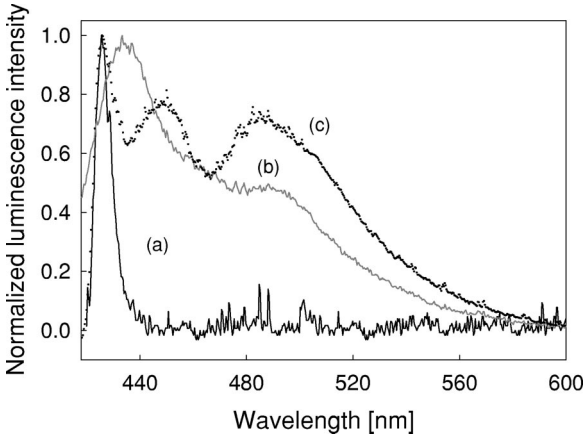

FIG. 3. Local spectra of luminescence intensity that is waveguided through a nanoscaled needle on mica. The solid line (a) is the spectrum obtained at the tip of the needle, 100 μm apart from a break. For comparison, the spectra of an ensemble of needles on mica [(b) gray curve] and a *p*-6P film on KCl [(c) dotted curve] are also shown.

structure by a fluorescence microscope and investigate the very same fibers with optical and local probe methods (viz., atomic force microscopy). The fluorescence microscope allows us to locally excite luminescence inside a selected needle and to spectroscopically determine the wavelength of the light that is propagating along the nanofiber. Deliberately induced, nanometer-sized breaks in the needles couple a constant fraction of the propagating light into the far field, the amount of which can be determined quantitatively as a function of distance between excitation and outcouple point. Since the breaks are of subwavelength size, damping of the propagating light by them is negligible. Damping in the present case is due to reabsorption inside the nanofibers.

On the basis of well-known classical electrodynamic waveguiding theory we have developed analytical expressions to describe optical waveguiding through our two-dimensionally confined nanofibers, which we apply to individually selected entities. From measurements of the damping of blue light in several different nanofibers, we evaluate the imaginary part of the dielectric function. Results are presented both for *p*-6P needles on single crystalline mica and on NaCl substrates.

II. EXPERIMENT

Needles of *para*-hexaphenyl are grown via evaporation of *p*-6P in vacuum (base pressure 1×10^{-9} mbar) with a rate of 0.025 nm/s on a freshly cleaved mica substrate, kept at 350 K surface temperature.[7] Both the deposition rate and the surface temperature are crucial parameters for the needle growth mode, determining height and mutual distance of the needles. The total deposited mass thickness, determined by a quartz microbalance, affects the length and—to a smaller extend—the width of the needles. Figure 2 shows typical fluorescence images of well-isolated needles grown in or near the focal area of an argon ion laser. Arrays of parallel needles with a well-defined length of 100 ± 20 μm can be generated as well as individual needles on different length scales.

The single crystallinity of the aggregates and the orientation of their unit cells are determined via low-energy electron diffraction with the help of a very low current channel plate LEED spectrometer. Since the generated patterns of organic aggregates on mica are stable against ambient air conditions, we can perform the optical and morphological characterization outside the growth chamber. We induce *p*-6*P* luminescence by focussing the 365-nm light of a high-pressure mercury lamp inside a microscope to a measured Gaussian focal radius of about 15 μm. A local spectroscopic analysis of the luminescence light from individual needles by a fiber-optic spectrometer results in a 0–1 band of the C-C stretch vibration at 425.5 nm [Fig. 3(a)]. This luminescence light is propagating along some of the needles. As can be seen by comparing the spectrum obtained at the tip of the needle, 100 μm apart from a break, with the spectra of an ensemble of needles on mica [Fig. 3(b)] and of a *p*-6P film on KCl [Fig. 3(c)], the light propagating in the nanofiber is spectrally significantly more confined. The measured spectral halfwidth is 6 nm.

Propagation of light inside the nanofibers is observed via nanometer-sized breaks which are deliberately induced by thermal stress in the course of the cooling process following preparation of the aggregates. Both the induced luminescence intensity at the primary spot of the exciting light and the outcoupled luminescence at the position of a break are quantitatively determined with the help of a charge-coupled device camera on top of the fluorescence microscope. The distance between excitation and outcoupling region is varied by a movable focusing lens and by moving the sample with micrometer precision. We have verified that the observed luminescence intensity is a linear function of excitation intensity for the moderate irradiances that we are applying in the present set up.

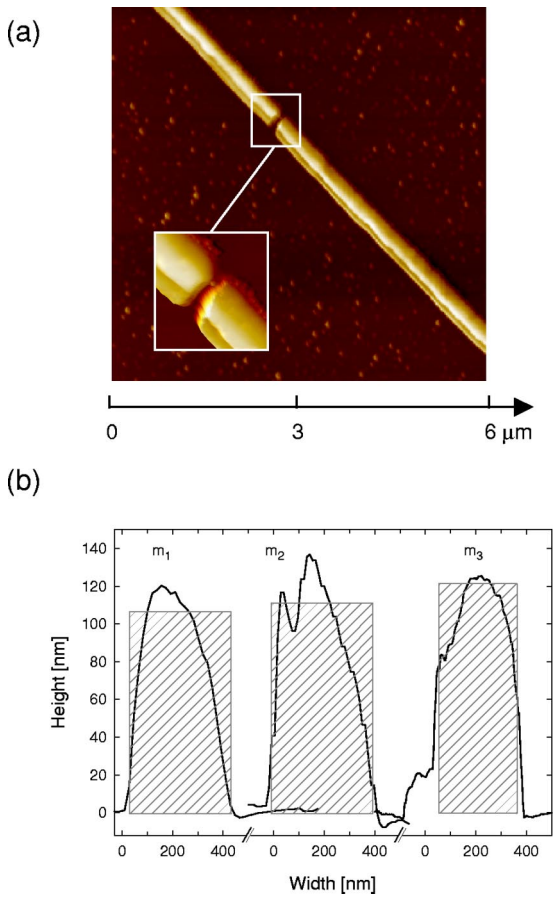

FIG. 4. (a) Force microscopy image ($5.9\times5.9\ \mu m^2$, deconvoluted from tip) of needle m_2. The inset is a blowup of the break region. Gap width is about 50 nm. (b) Height scans through nanofibers m_1, m_2, and m_3 on mica, revealing typical dimensions. The shaded boxes have widths of 400 nm (m_1), 400 nm (m_2), and 300 nm (m_3), respectively.

From the characteristic appearance of the environment around selected needles [demonstrated in Fig. 2(b)] it is possible to identify and to locate a single needle by optical microscopy. This allows us to characterize the same needles by atomic force microscopy (AFM) as were measured by optical fluorescence methods. Alignment of the needle under the AFM tip was controlled by microscopically observing the sample and the cantilever from below through a transparent sample holder. The AFM was done with a PicoSPM (molecular imaging) operated in tapping mode. In Figs. 4, 5, and 7, we show force microscopy images of selected nanofibers on mica and on NaCl. For further reference, we label the needles m_1, m_2, and m_3 (needles on mica), as well as n_1 (needle on NaCl). The AFM allows us to deduce typical dimensions that are critical for the waveguiding process, as demonstrated by several height scans through the needles.

III. THEORY

Let us approximate the nanofiber by a rectangular waveguide with sides a along the x axis and b along the y axis, placed on a dielectric substrate (Fig. 6). The dielectric constants of the medium surrounding the waveguide (medium 1) and the substrate (medium 3) are ϵ_1 and ϵ_3, respectively, and the waveguide interior (medium 2) is optically uniaxial with the dielectric permittivity tensor

$$\hat{\epsilon}_2 = \begin{pmatrix} \epsilon_\parallel & 0 & 0 \\ 0 & \epsilon_\perp & 0 \\ 0 & 0 & \epsilon_\perp \end{pmatrix}. \tag{1}$$

We assume that the dielectric constants ϵ_1 and ϵ_3 are real and $\epsilon_1 < \epsilon_3$. The imaginary parts of $\epsilon_\perp$ and $\epsilon_\parallel$ are much less than their real parts and $\epsilon_\perp < \epsilon_\parallel$ and the magnetic permeability $\mu = 1$ in all three media.

From the Maxwell equation for the electric field in the waveguide interior, we derive

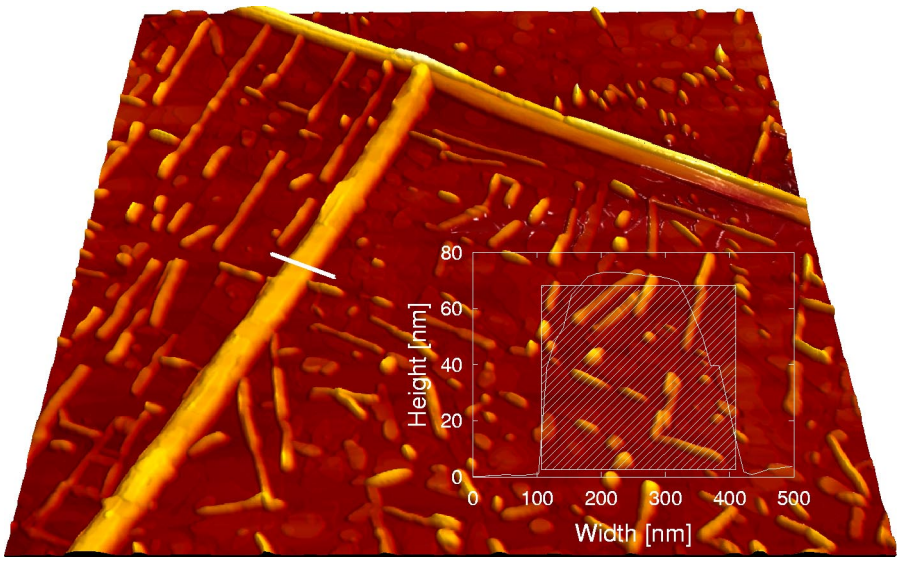

FIG. 5. Deconvoluted force microscopy image of nanofibers on NaCl. Image size $6.5\times6.5\ \mu m^2$, width of the shaded box 300 nm.

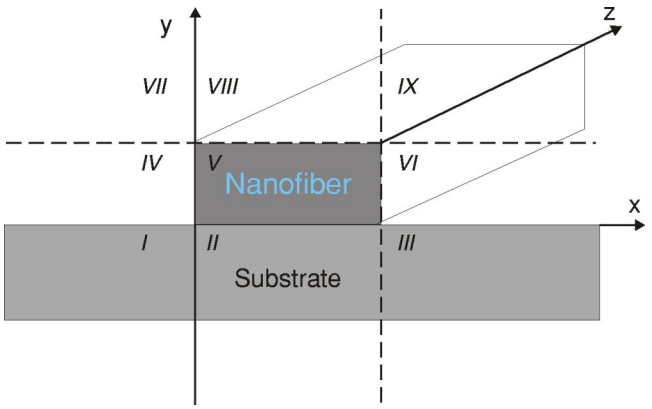

FIG. 6. Geometry for the theoretical evaluation of the needles, denoting the nine different regions that surround the nanowaveguide.

$$\nabla \cdot \mathbf{E} = -\frac{\epsilon_{\parallel} - \epsilon_{\perp}}{\epsilon_{\perp}} \frac{\partial E_x}{\partial x}. \tag{2}$$

and thus obtain the wave equation

$$\left(\gamma_j \frac{\partial^2}{\partial x^2} + \frac{\partial^2}{\partial y^2} + \frac{\partial^2}{\partial z^2} - \frac{1}{c_j^2} \frac{\partial^2}{\partial t^2} \right) E_{xj} = 0, \tag{3}$$

where the index j represents the index of the medium, $\gamma_1 = \gamma_3 = 1$, $\gamma_2 = \epsilon_{\parallel}/\epsilon_{\perp}$, $c_1 = c/\sqrt{\epsilon_1}$, $c_2 = c/\sqrt{\epsilon_{\parallel}}$, $c_3 = c/\sqrt{\epsilon_3}$ with c the speed of light in vacuum.

We shall seek the solution for the field amplitudes in the form

$$F_{\alpha j}(x,y,z) = F^0_{\alpha j}(x,y) \exp[i(\omega t - \beta z)], \tag{4}$$

where F_{α} is a component of the electric or magnetic field ($\alpha = x,y,z$), ω and β are the wave frequency and propagation constant, respectively.

In the Appendix it is shown that TE waves cannot exist in nanofiber waveguides of the kind we are employing. The electric-field vector of the waveguiding TM modes lies in the xz plane. From Eq. (A42), we find the cutoff frequency for TM waves

$$\omega_c = \frac{c}{\sqrt{\epsilon_{\perp}}} \frac{m\pi}{a} \tag{5}$$

and the cutoff wavelength

$$\lambda_c = \frac{2\sqrt{\epsilon_{\perp}}a}{m}. \tag{6}$$

The number of possible modes is restricted by the condition that the field amplitude must decrease when one moves away from the waveguide [see Eqs. (A32) and (A33)]. As it follows from Eq. (A17) for $j = 3$, one has $\beta > k_3$ and therefore the following condition should hold:

$$m < \frac{2a}{\lambda} \sqrt{\frac{\epsilon_{\perp}}{\epsilon_{\parallel}}} \sqrt{\epsilon_{\parallel} - \epsilon_3}, \tag{7}$$

with λ the wavelength of the propagating light.

IV. COMPARISON WITH EXPERIMENT

For a quantitative theoretical prediction of the waveguiding behavior of the nanofibers, we use the values of $\epsilon_1 = 1$, $\gamma_2 = 2.5$,[11] $\sqrt{\epsilon_3} = 1.58$ for mica and $\sqrt{\epsilon_3} = 1.57$ for NaCl. The value of the refractive index for an isotropic *para*-hexaphenyl film is $\sqrt{\epsilon_2} = 1.7$ for[12] $\lambda = 425$ nm and, thus, $\epsilon_{\perp} = 1.9$ and $\epsilon_{\parallel} = 4.8$. Typical widths for nanofibers on mica are $a = 400$ nm [Fig. 4(b), needles m_1 and m_2] and for NaCl $a = 300$ nm (Fig. 5). For $\lambda = 425$ nm (Fig. 3) and using Eq. (7) it follows that the minimum needle width at which at least one mode can propagate along the needle is $a_1 = 222$ nm. The second mode appears at $a_2 = 444$ nm.

In Fig. 7, we present a force microscopy image of a fiber with a single break, where waveguiding was observed on one side of the break but not on the other. Height scans along the opposite ends of the image show that the nonwaveguiding part [Fig. 7(a)] has a significantly narrower cross section as compared to the waveguiding part opposite to the break [Fig. 7(b)]. The shaded box in Fig. 7(a) has a width corresponding to the lower theoretical threshold for waveguiding ($a = 222$ nm), whereas that in Fig. 7(b) corresponds to waveguiding in the lowest-order TM mode ($a = 400$ nm). Thus, the analytical theory agrees with the optical and morphological findings. The cutoff wavelengths are $\lambda_c = 1103$ nm for $a = 400$ nm and $\lambda_c = 827$ nm for $a = 300$ nm. Therefore, even infrared light is transmitted through the nanofiber.

Now let us turn to an investigation of damping of propagating light modes in the nanofibers. Fluorescence images of

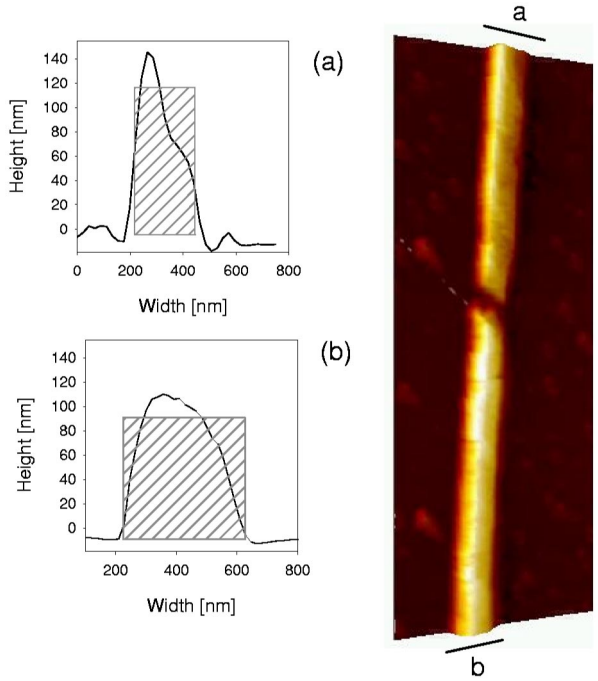

FIG. 7. Force microscopy image ($1.5 \times 4\ \mu m^2$) of a *p*-6P nanofiber (needle m_1) in the neighborhood of a break (150 nm wide). The upper part (a) is not waveguiding, the lower (b) is. On the left-hand-side height scans through the upper and lower parts are shown. The gray shaded boxes have widths of 222 nm and 400 nm, respectively.

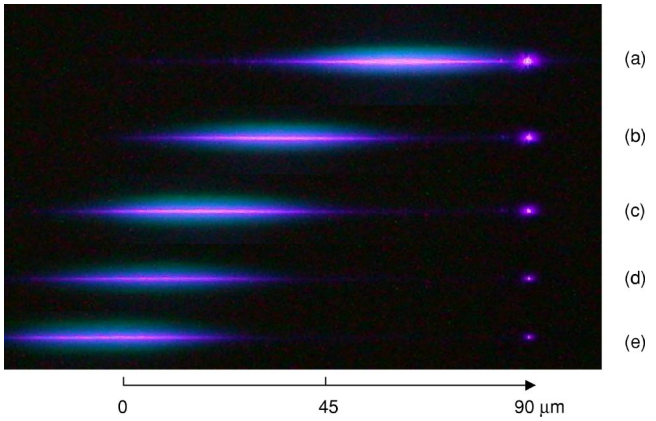

FIG. 8. Five fluorescence images of needle m_1 following local excitation for increasing distances (a)–(e) between excitation and outcoupling points.

outcoupled intensity at the break for increasing distances between excitation and outcoupling points are shown in Fig. 8. The classical theory predicts the intensity of the guided wave to decrease exponentially with distance along the waveguide, i.e.,

$$I(z) = I(z_0)\exp[2\ \mathrm{Im}\beta(z - z_0)], \tag{8}$$

the imaginary part of the propagation constant being determined by the imaginary parts of the waveguide dielectric tensor components. We believe that the losses in a needle are mainly due to absorption by hexaphenyl molecules which occur if the electric-field vector of the light is directed along the molecular axes. According to that we assume that only the $\epsilon_\parallel$ component possesses an imaginary part (i.e., $\epsilon_\parallel = \epsilon'_\parallel - i\epsilon''_\parallel$), whereas the imaginary part of $\epsilon_\perp$ can be neglected. The quantity $\epsilon''_\parallel$ is an adjustable parameter, which we will determine by a direct comparison of experiment and theory.

Figures 9 and 10 show measured and calculated dependencies of the intensity scattered at the needle breaks on the distance between the center of the excitation spot and the breaks. For the needles on mica, we get $\epsilon''_\parallel = 0.009 \pm 0.001$ [m_1, a given by the width of the box in Fig. 4(b)], $\epsilon''_\parallel = 0.014 \pm 0.002$ (m_2, $a = 400$ nm) and $\epsilon''_\parallel = 0.012 \pm 0.001$ (m_3, $a = 300$ nm), whereas for the needle on a NaCl substrate $\epsilon''_\parallel = 0.0136 \pm 0.0009$ (n_1, Fig. 5, $a = 300$ nm). The mean value for all measured needles is $\epsilon''_\parallel = 0.012 \pm 0.002$.

Density-functional calculations for the hexaphenyl bulk provide for the $\epsilon''_{\parallel\mathrm{cryst}}$ component of the dielectric function a singularity at the band edge (0-0) with an amplitude of about 30.[13] The band edge corresponds to the electronic transition from the lowest vibrational state of the ground electronic state to the excited electronic state of hexaphenyl molecules. Hence, we expect for the corresponding component of a fiber on a substrate at $T_S = 300$ K: $\epsilon''_\parallel = \epsilon''_{\parallel\mathrm{cryst}} \times F_B \times \Delta$. Here, F_B denotes the relative population of the first excited vibrational state of the ground electronic state, which determines the absorption at 425.5 nm. Given the vibrational excitation energy to be 182 meV,[14] the corresponding Boltzmann factor is 8.6×10^{-4}. The influence of the finite size of the fiber on $\epsilon''_\parallel$ is reflected in the factor $\Delta = \delta_{\mathrm{fiber}}/\delta_{\mathrm{cryst}} = 0.462$, where δ_{fiber} and δ_{cryst} are the spectral linewidths of the fiber and the crystal, see Fig. 3. The final estimate for a p-6P fiber is $\epsilon''_\parallel \sim 0.0119$, which agrees well with the values obtained from the fitting of spatial luminescence decay.

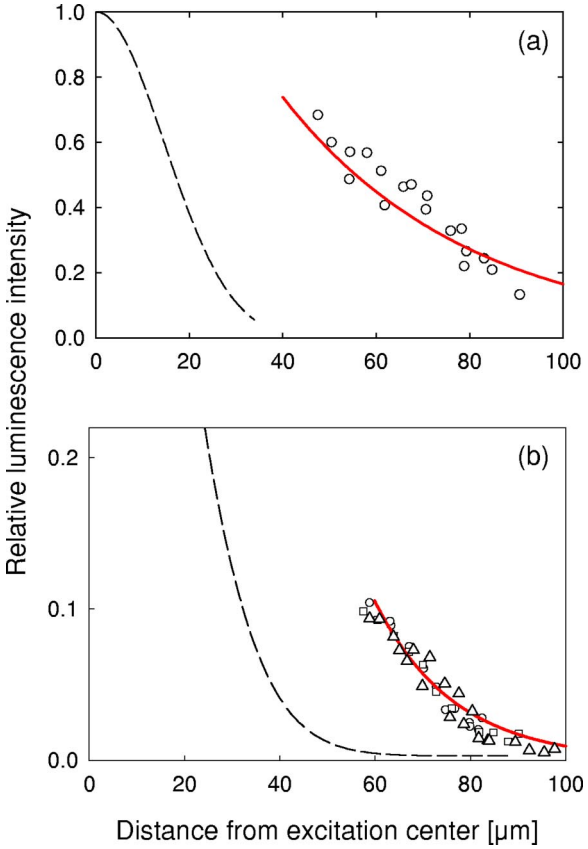

FIG. 9. (a) Outcoupled luminescence intensity as a function of distance from the excitation point for an individual needle on mica (needle m_1). The dashed line represents the spatial excitation profile. The continuous solid line is a fit using $\epsilon''_\parallel = 0.009 \pm 0.001$. (b) Same as (a), but for needle m_2 on mica ($\epsilon''_\parallel = 0.014 \pm 0.002$).

V. CONCLUSIONS

In this paper, we have presented experimental data together with a quantitative theoretical evaluation of single-mode optical waveguiding of blue light (425 nm) through nanoscaled dielectric fibers of hexaphenyl oligomers. Blue light is especially useful for high-density information storage and treatment on future submicron-sized optoelectronic components.

The nanofibers have been generated on mica and NaCl single crystalline surfaces by laser-assisted self-assembly. The self-assembly process leads via a strong dipole-induced dipole interaction to arrays of mutually parallel oriented entities which emit highly polarized blue light. Since the growth process depends substantially on deposition conditions and on thermal surface gradients, the topology of individual fibers as well as the overall size distribution can be varied by application of local laser heating. This new kind of nanoscaled waveguides possess the advantageous properties

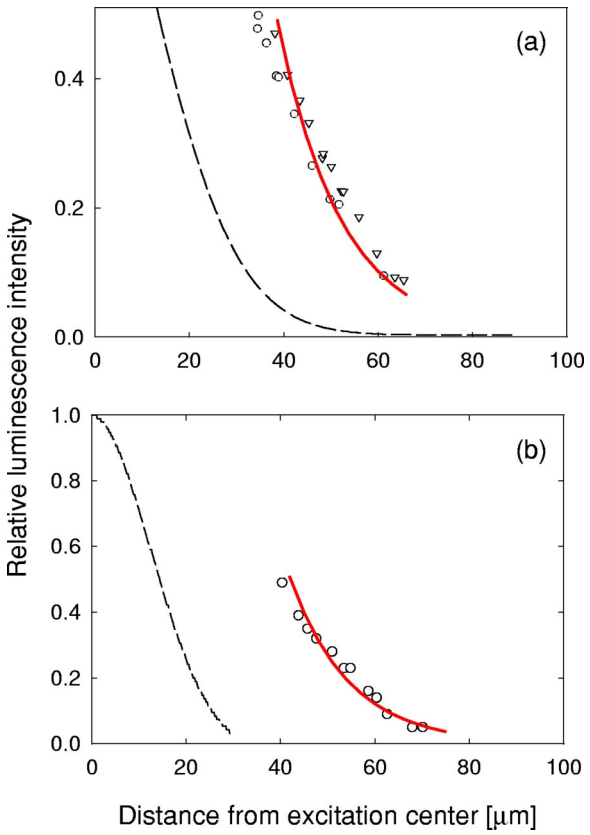

FIG. 10. (a) Same as Fig. 9, but for needle m_3 on mica ($\epsilon_{\parallel}''=0.012\pm0.001$). (b) Same as (a), but for a needle on NaCl (needle n_1, $\epsilon_{\parallel}''=0.0136\pm0.0009$).

of being of correct size in one important dimension to allow optical waveguiding, while they are extendable to millimeter size in another dimension[15] and are flat on a nanometer scale over their whole surface area. As proven by low-energy electron diffraction, the nanofibers are single crystalline with well-defined orientations of the individual *para*-hexaphenyl molecules with respect to the fiber axis. The identification of the same nanofibers in an optical fluorescence microscope and an atomic force microscope has allowed us to perform local spectroscopy and luminescence damping measurements on morphologically well-characterized individual aggregates.

The presented analytical theory describes the waveguiding conditions satisfactorily, especially the tunability of the waveguiding properties by modifying the dimensions of the needles. From a comparison of measured and predicted damping of the TM waves propagating along the nanofibers, we obtain the parallel component of the imaginary part of the fibers dielectric function, $\epsilon_{\parallel}''=0.012\pm0.002$.

Waveguiding along the nanofibers is expected to be restricted mainly by (i) the cutoff wavelength given by the dimensions of the waveguide and (ii) damping of the propagating light. If one is interested in guiding infrared light of 1.3 μm, this should be possible with nanofibers having widths $a=470$ nm. Damping is especially pronounced in the blue spectral range since it is caused by reabsorption of the propagating light. For wavelengths above 550 nm reabsorption becomes negligible and scattering losses will dominate. Due to the high optical quality of the nanofibers in terms of surface roughness [cf. Fig. 4(a)] scattering losses should be small, but this has to be investigated quantitatively in a separate study. On the other hand, one experiences often impurity-induced absorption bands in the optical band gap in conjugated organic molecules, which would decrease the possible propagation length of the guided light again. While we have no direct hint for such an effect in the present nanofibers, there is also no fundamental reason which would limit our growth control method to conjugated organic molecules.

ACKNOWLEDGMENTS

We thank the Danish Research Agency SNF for funding this work and also NATO for a collaborative linkage grant. A.C.S. is grateful to the Danish National Research Foundation for support via a grant to the MEMPHYS-Center for Biomembrane Physics.

APPENDIX

1. TE waves

We discuss first transverse electric (TE) waves for which $E_z=0$. From Maxwell's equations one gets the following relations between the magnetic- and electric-field components:

$$H_y^0(x,y)=\frac{c}{\omega}\beta E_x^0(x,y), \tag{A1}$$

$$H_x^0(x,y)=-\frac{c}{\omega}\beta E_y^0(x,y), \tag{A2}$$

$$\frac{\partial H_y^0(x,y)}{\partial x}=\frac{\partial H_x^0(x,y)}{\partial y}. \tag{A3}$$

As a consequence, we have

$$\nabla\cdot\mathbf{E}=0. \tag{A4}$$

Hence, from Eq. (2) it is concluded that inside the waveguide

$$\frac{\partial E_x^0(x,y)}{\partial x}=0. \tag{A5}$$

The boundary conditions require continuity of the components H_y and D_x for movement along the x axis across the boundary between the media 1 and 2. Thus, the following relations should hold:

$$H_{y1}^0(0,y)=H_{y2}^0(0,y), \tag{A6}$$

$$\epsilon_1 E_{x1}^0(0,y)=\epsilon_{\parallel}E_{x2}^0(0,y). \tag{A7}$$

Taking into account Eq. (A1), we get the condition

$$E_{x1}^0(0,y)=E_{x2}^0(0,y)=0. \tag{A8}$$

Now combining Eqs. (A5) and (A8), we find that $E_x^0=0$ inside the waveguide. This is also valid for the medium surrounding the waveguide as the field amplitude should equal zero at infinite distance from it. Analogously, we get $E_y^0=0$, i.e., TE waves cannot exist in such nanofiber waveguides.

2. TM waves

Let us now turn to transverse magnetic (TM) waves for which $H_z=0$. Maxwell's equations lead to the following relations between the field components in the waveguide interior:

$$H_{y2}^0(x,y)=\frac{\omega\epsilon_\parallel}{c\beta}E_{x2}^0(x,y), \tag{A9}$$

$$H_{x2}^0(x,y)=-\frac{\omega\epsilon_\perp}{c\beta}E_{y2}^0(x,y), \tag{A10}$$

$$\frac{\partial E_{x2}^0(x,y)}{\partial y}=\frac{\partial E_{y2}^0(x,y)}{\partial x}, \tag{A11}$$

$$\frac{\partial H_{x2}^0(x,y)}{\partial x}=-\frac{\partial H_{y2}^0(x,y)}{\partial y}. \tag{A12}$$

As a consequence one obtains the equation

$$\frac{1}{\epsilon_\perp}\frac{\partial H_{y2}^0(x,y)}{\partial y}=\frac{1}{\epsilon_\parallel}\frac{\partial H_{y2}^0(x,y)}{\partial y}, \tag{A13}$$

with the solution

$$\frac{\partial H_{y2}^0(x,y)}{\partial y}=0, \tag{A14}$$

that leads to the condition inside the waveguide

$$\frac{\partial E_{x2}^0(x,y)}{\partial y}=\frac{\partial E_{y2}^0(x,y)}{\partial x}=0. \tag{A15}$$

Substituting expression (4) into equation (3), we get the equation

$$\left(\gamma_j\frac{\partial^2}{\partial x^2}+\frac{\partial^2}{\partial y^2}+h_j^2\right)E_{xj}^0(x,y)=0, \tag{A16}$$

where we have introduced the notation

$$h_j^2=k_j^2-\beta^2, \tag{A17}$$

with $k_j=\omega/c_j$.

In Eq. (A16) the variables can be separated by letting

$$E_{xj}^0(x,y)=X_j(x)Y_j(y), \tag{A18}$$

where the functions X_j and Y_j satisfy the equations

$$\frac{d^2X_j(x)}{dx^2}+\tilde{q}_{xj}^2X_j(x)=0 \tag{A19}$$

and

$$\frac{d^2Y_j(y)}{dy^2}+q_{yj}^2Y_j(y)=0, \tag{A20}$$

with

$$\tilde{q}_{xj}^2=\frac{1}{\gamma_j}q_{xj}^2 \tag{A21}$$

and

$$q_{xj}^2+q_{yj}^2=h_j^2. \tag{A22}$$

Let us divide the whole space containing the waveguide into nine regions as it is shown in Fig. 6 and consider the solution of Eq. (A16) for each region. Taking into account Eq. (A15), we conclude that the fundamental solutions in the region II corresponding to the waveguiding modes are $\sin(\tilde{q}_{x2}x)$ and $\cos(\tilde{q}_{x2}x)$. One can compose them of the odd and even modes with respect to the plane $x=a/2$.

Consider first the odd TM modes. In this case, the solutions in the different regions which vanish at infinite distance from the waveguide have the form

$$E_x^I=A_I\exp(\kappa_{x3}x)\exp(\kappa_{y3}y), \tag{A23}$$

$$E_x^{II}=A_{II}\sin\left[q_{x3}\left(x-\frac{a}{2}\right)\right]\exp(\kappa_{y3}y), \tag{A24}$$

$$E_x^{III}=A_{III}\exp[-\kappa_{x3}(x-a)]\exp(\kappa_{y3}y), \tag{A25}$$

$$E_x^{IV}=A_{IV}\exp(\kappa_{x1}x), \tag{A26}$$

$$E_x^{V}=A_V\sin\left[\tilde{q}_{x2}\left(x-\frac{a}{2}\right)\right], \tag{A27}$$

$$E_x^{VI}=A_{VI}\exp[-\kappa_{x1}(x-a)], \tag{A28}$$

$$E_x^{VII}=A_{VII}\exp(\kappa_{x1}x)\exp[-\kappa_{y1}(y-b)], \tag{A29}$$

$$E_x^{VIII}=A_{VIII}\sin\left[q_{x1}\left(x-\frac{a}{2}\right)\right]\exp[-\kappa_{y1}(y-b)], \tag{A30}$$

$$E_x^{IX}=A_{IX}\exp[-\kappa_{x1}(x-a)]\exp[-\kappa_{y1}(y-b)], \tag{A31}$$

where we have introduced the notations ($j=1,3$)

$$\kappa_{xj}^2=-q_{xj}^2,\quad \mathrm{Re}(\kappa_{xj})>0, \tag{A32}$$

$$\kappa_{yj}^2=-q_{yj}^2,\quad \mathrm{Re}(\kappa_{yj})>0. \tag{A33}$$

Since continuity of the E_x component at all the boundaries between the regions except $IV-V$ and $V-VI$ has to be fulfilled, we get the following equations:

$$q_{x1}=\tilde{q}_{x2}=q_{x3}, \tag{A34}$$

$$A_I = -A_{II}\sin\left(\tilde{q}_{x2}\frac{a}{2}\right) = -A_{III} = A_{IV} = -A_V\sin\left(\tilde{q}_{x2}\frac{a}{2}\right)$$

$$= -A_{VI} = A_{VII} = -A_{VIII}\sin\left(\tilde{q}_{x2}\frac{a}{2}\right) = -A_{IX}. \quad \text{(A35)}$$

The continuity of the D_x component at the boundaries $IV-V$ and $V-VI$ leads to the equation

$$\epsilon_1 A_{IV} = -\epsilon_\parallel A_V \sin\left(\tilde{q}_{x2}\frac{a}{2}\right). \quad \text{(A36)}$$

Comparing Eqs. (A35) and (A36), we conclude that a nontrivial solution is possible only if

$$\sin\left(\tilde{q}_{x2}\frac{a}{2}\right) = 0, \quad \text{(A37)}$$

or

$$\tilde{q}_{x2} = \frac{2m\pi}{a}, \quad \text{(A38)}$$

with $m = 1,2,3,\ldots$. In this case only the coefficients $A_{II} = A_V = A_{VIII}$ are nonzero. Quite analogously one finds that even TM modes can exist only if

$$\cos\left(\tilde{q}_{x2}\frac{a}{2}\right) = 0, \quad \text{(A39)}$$

or

$$\tilde{q}_{x2} = \frac{(2n+1)\pi}{a}, \quad \text{(A40)}$$

with $n = 0,1,2,\ldots$. Now combining Eqs. (A40) and (A38), we infer that TM modes exist if

$$\tilde{q}_{x2} = \frac{m\pi}{a}, \quad \text{(A41)}$$

where $m = 1,2,3,\ldots$.

The corresponding propagation constant can be obtained from Eqs. (A17), (A21), and (A22) with $q_{y2} = 0$:

$$\beta = \left[\frac{\omega^2}{c^2}\epsilon_\parallel - \frac{\epsilon_\parallel}{\epsilon_\perp}\left(\frac{m\pi}{a}\right)^2\right]^{1/2}. \quad \text{(A42)}$$

Let us consider now the other two components of the electric-field vector E_y and E_z. The continuity of E_y and H_x at the boundary $IV-V$ requires that

$$E^0_{y1}(0,y) = E^0_{y2}(0,y), \quad \text{(A43)}$$

$$\epsilon_1 E^0_{y1}(0,y) = \epsilon_\perp E^0_{y2}(0,y), \quad \text{(A44)}$$

which leads to the condition

$$E^0_{y2}(0,y) = 0. \quad \text{(A45)}$$

On the other hand, the component E^0_y does not depend on x inside the waveguide [see Eq. (A15)]. Therefore, we have $E^0_y = H^0_x = 0$ in the waveguide interior and hence in the whole space. Now from the Maxwell equation for $\nabla \times \mathbf{H}$ one gets

$$E^0_{zj}(x,y) = -i\frac{\gamma_j}{\beta}\frac{\partial E^0_{xj}(x,y)}{\partial x}. \quad \text{(A46)}$$

Thus, the electric-field vector of the waveguiding modes lies in the xz-plane.

*Electronic address: rubahn@fysik.sdu.dk

[1] J. Foresi, P. Villeneuve, J. Ferrera, E. Thoen, G. Steinmeyer, S. Fan, J. Joannopoulos, L. Kimerling, H. Smith, and E. Ippen, Nature (London) **390**, 143 (1997).
[2] M. Notomi, K. Yamada, A. Shinya, J. Takahashi, C. Takahashi, and I. Yokohama, Phys. Rev. Lett. **87**, 253902 (2001).
[3] F. Balzer, V. Bordo, A. Simonsen, and H.-G. Rubahn, Appl. Phys. Lett. **82**, 10 (2003).
[4] E. Zojer *et al.*, Phys. Rev. B **61**, 16 538 (2000).
[5] N. Tessler, Adv. Math. **11**, 363 (1999).
[6] H. Yanagi and S. Okamoto, Appl. Phys. Lett. **71**, 2563 (1997).
[7] F. Balzer and H.-G. Rubahn, Appl. Phys. Lett. **79**, 3860 (2001).
[8] F. Balzer and H.-G. Rubahn, Surf. Sci. **507**, 588 (2002).
[9] H. Plank, R. Resel, S. Purger, J. Keckes, A. Thierry, B. Lotz, A. Andreev, N.S. Sariciftci, and H. Sitter, Phys. Rev. B **64**, 235423 (2001).
[10] F. Balzer and H.-G. Rubahn, Nano Lett. **2**, 747 (2002).
[11] C. Ambrosch-Draxl, J.A. Majewski, P. Vogl, and G. Leising, Phys. Rev. B **51**, 9668 (1995).
[12] A. Niko, S. Tasch, F. Meghdadi, C. Brandstätter, and G. Leising, J. Appl. Phys. **82**, 4177 (1997).
[13] P. Puschnig and C. Ambrosch-Draxl, Phys. Rev. B **60**, 7891 (1999).
[14] H. Yanagi, T. Ohara, and T. Morikawa, Adv. Math. **13**, 1452 (2001).
[15] By growth of the nanofibers across domain boundaries it is also possible to fabricate bent nanofibers.